

Evidence on the Orbital Modulated Gamma-Ray Emissions from the Redback Candidate 3FGL J2039.6-5618

C. W. Ng¹, J. Takata², J. Strader³, K. L. Li³, and K. S. Cheng¹

Department of Physics, The University of Hong Kong, Pokfulam Road, Hong Kong

School of Physics, Huazhong University of Science and Technology, Wuhan 430074, People's Republic of China; takata@hust.edu.cn

Department of Physics and Astronomy, Michigan State University, East Lansing, MI 48824, USA

Received 2018 June 5; revised 2018 September 17; accepted 2018 September 18; published 2018 November 2

Abstract

Using 9.5 yr of *Fermi* Large Area Telescope data, we report the evidence on the orbital modulated gamma-ray emissions from the redback candidate 3FGL J2039.6–5618. We produced the folded light curve with the orbital period of \sim 5.47 hr at a \sim 4 σ level. We also computed the gamma-ray spectra in two orbital phases corresponding to the inferior conjunction and the superior conjunction. We found that the <3 GeV excess in the spectrum of inferior conjunction can be modeled by the inverse Compton scattering between a relativistic pulsar wind and background soft photons of the companion star. The orbital modulation can also be explained by the evolving collision angle between the particles and photons in the same model. Through period searches by the Rayleigh test and the flux variability, we speculate that the orbital modulation is not detected after MJD \sim 57,000. We propose a possible explanation in which the intrabinary shock is located closer to the pulsar so that the pulsar wind carries a smaller Lorentz factor. We estimated that the resultant inverse Compton component will be too soft and too weak to be observed.

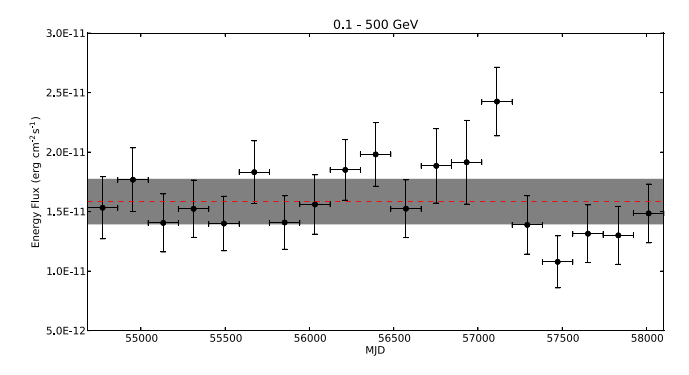
Key words: binaries: close – gamma rays: stars – pulsars: individual (3FGL J2039.6–5618) – stars: neutron

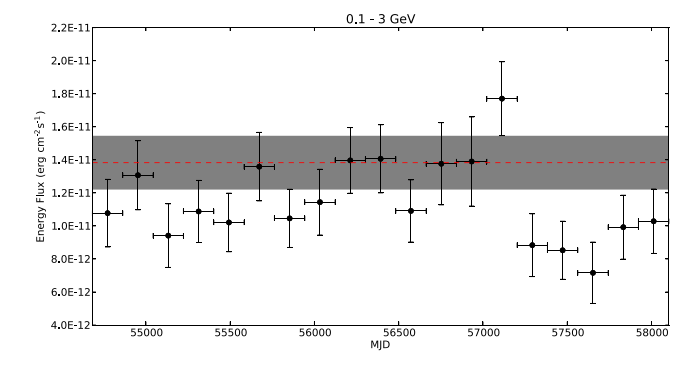
1. Introduction

A redback is a closed millisecond pulsar binary orbiting with a low-mass companion main-sequence star of $\sim 0.1-0.4 M_{\odot}$. The system is so compact that the typical orbital period is only 0.1-1.0 day. One distinctive feature of redback systems is the mass ablation of the companion star. As the companion is orbiting around the millisecond pulsar, the pulsar powers energetic radiation that shines on the surface of the companion and causes the facing side to be heated up. As a result, the star experiences continuous mass loss, and it can be eventually "evaporated" (Chen et al. 2013). These redback systems can be observed in optical, X-ray, and gamma-ray bands. In optical, because of the heating by the pulsar irradiation, the star becomes more luminous when the facing side is visible at the superior conjunction (where the pulsar is located between the companion and the observer), and it appears dimmer at the opposing inferior conjunction (where the star is located between the pulsar and the observer). In X-ray, the orbital modulated contribution is a result of the relativistic Doppler boosting at the intrabinary shock (Huang et al. 2012), which probably bows around the millisecond pulsar. Finally, the orbital modulating gamma ray could be generated from the inverse Compton (IC) scattering, in which the stellar soft photons gain energy from relativistic pulsar wind charged particles. This process is dependent on the collision angle; thus, the emission is the strongest at the inferior conjunction owing to head-on collisions and the weakest at the superior conjunction owing to tail-on collisions.

The Fermi Gamma-ray Space Telescope, launched in 2008, provides high-quality all-sky observations on space gamma rays that are crucial for studying high-energy astronomy. The target of this paper, 3FGL J2039.6–5618, is an unassociated gamma-ray source published in the third point-source catalog (3FGL) of the Fermi Large Area Telescope (LAT; Acero et al. 2015). Later, Salvetti et al. (2015) and Romani (2015)

performed independent X-ray and optical observations on this source and revealed its orbital modulating features. Thus, they suggested it to be a new redback pulsar binary candidate. In the study performed by Salvetti et al. (2015), they used X-ray observations from XMM-Newton and discovered that there is a bright X-ray counterpart within the gamma-ray error circle at the location of 3FGL J2039.6-5618. This X-ray source is variable with a period of 0.2245 \pm 0.0081 days. They also presented results from the GROND observation, which shows that the optical counterpart has a periodicity at $P = 0.22748 \pm 0.00043$ days, which is consistent with the result in the X-ray band. On the other hand, Romani (2015) further refined the orbital period to 0.228116 \pm 0.000002 days using GHTS and DES observations in the optical band, together with the barycentric epoch of optical maximum identified at MJD 56,885.065. This short orbital period of 5.47 hr implies that the binary system is compact, and therefore it is likely a redback. Furthermore, from the orbit modeling on the observed data, Salvetti et al. (2015) reported that the best-fit epoch of quadrature of the binary is MJD 56,884.9667 ± 0.0003 , and they suggested that the companion star is experiencing large deformation. On the other side, the modeling by Romani (2015) indicates that the mass of the companion star has an upper limit of $\leq 0.61 \, M_{\odot}$ and the effective temperature is ~4200 K. In the gamma-ray observation by the Fermi-LAT, this source is showing a consistent luminosity throughout the mission. The gamma-ray spectrum of 3FGL J2039.6-5618 is curved, making it consistent with the spectrum of a typical millisecond pulsar. However, the exact claim on the pulsar nature of the source cannot be produced currently because no radio or gamma-ray pulsations have ever been detected. In this study, we further analyze the Fermi-LAT data of 3FGL J2039.6-5618 to explore the nature of this target in high energy and to find indications of orbital modulations in gamma rays, which is the final expectation from our understanding on the redback systems.





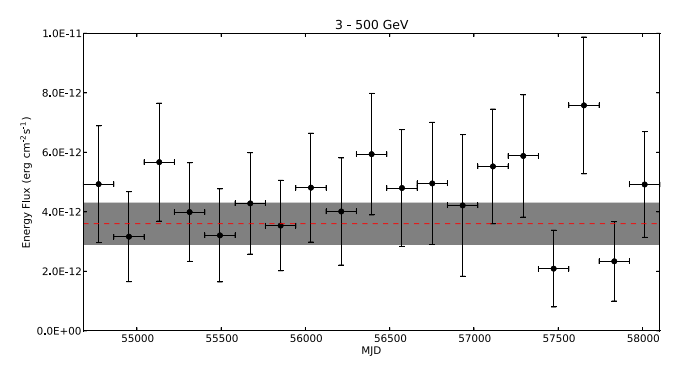


Figure 1. Energy flux of 3FGL J2039.6–5618 during the \sim 9.5 yr of *Fermi* mission in energy ranges of 0.1–500 GeV (top), 0.1–3 GeV (middle), and 3–50 GeV (bottom). The red dashed line represents the best-fit overall energy flux. The gray band represents the corresponding uncertainty.

2. Data Analysis

We analyzed the *Fermi* gamma-ray data of 3FGL J2039.6–5618 by the *Fermi* Science Tools package version v10r0p5.⁴ The "Pass 8 Source" class photon events from 2008 August 04 to 2018 January 30 were selected in the energy range from 100 MeV to 500 GeV. The corresponding instrumental response function is "P8R2_SOURCE_V6." The region of interest (ROI) is a $20^{\circ} \times 20^{\circ}$ square centered at the epoch J2000 position of the source: (R.A., decl.) = $(20^{\rm h}39^{\rm m}35^{\rm s}.21, -56^{\circ}16'55.$ "6). To reduce contaminations from Earth's albedo, time intervals in which the ROI is observed at a zenith angle greater than 90° were excluded. The background model includes all the 3FGL catalog sources (gll_psc_v16.fit; Acero et al. 2015) that are within 25° from the center of ROI, the galactic diffuse emission (gll_iem_v06), and the isotropic diffuse emission (iso_P8R2_SOURCE_V6_v06), available from the *Fermi* Science Support Center (FSSC). The

spectral parameters for sources that are nonvariable and located 5° away from the center are fixed to their catalog values. The *gtlike* tool (Binned Likelihood) was used to optimize the spectral parameters in the background model for this data set.

2.1. Flux Variability

The time series of the energy flux of 3FGL J2039.6–5618 was computed by splitting the ~ 9.5 yr of data into 180-day intervals. Spectral indices in the spectral model were fixed to their best-fit values for all data, leaving only the normalization parameters free. The values of the normalizations were determined by binned likelihood analysis in each time interval. Figure 1 shows the resulting time series in three energy ranges we considered: $0.1-500~{\rm GeV}$ (top), $0.1-3~{\rm GeV}$ (middle), and $3-500~{\rm GeV}$ (bottom). Note that although the $0.1-500~{\rm GeV}$ energy flux remains generally constant for most of the observation, the flux around MJD 57,000 is 4 standard deviations above the average. This increase is most likely to be due to the lower energy $<3~{\rm GeV}$. We will revisit this feature in the next section.

2.2. Orbital Light Curve

The orbital period of 3FGL J2039.6-5618 is recently revised by J. Strader et al. (2018, in preparation) to be $P_{\text{Strader}} =$ 0.2279817(7) days. Using this value as a reference, we searched for orbital modulation from the gamma-ray data. Since we expect that the gamma-ray modulation originated from the IC scattering between the pulsar wind and the stellar soft photons, the pulse profile would behave as a single-peak pulsation. Therefore, the Rayleigh test (Brazier 1994) from the gtpsearch tool is used to search for the orbital period. In this timing analysis, we further selected the photons from a smaller ROI of 0.6 radius centered at the specified source coordinates. Using 3×10^{-12} Hz as the resolution in the frequency domain, we set 10,000 trial frequencies around $f_0 = 5.076754 \times 10^{-5}$ Hz for the search. Figure 2(a) shows the power spectrum of the Rayleigh test for the full data set. The best frequency is $f_{\text{full}} = 5.076889(3) \times 10^{-5} \,\text{Hz}$ (in period, $P_{\text{full}} = 0.227975(7) \text{ days}$ at a test-statistic of $\chi^2 = 25.2$ with two degrees of freedom. This is equivalent to a \sim 4.64 σ significance. As we noted from the long-term light curve in Section 2.1, the source shows a possible variability around MJD 57,000. We speculate that the system may have experienced some changes in the timing parameters as well. Therefore, we did the frequency search again in two periods of time: before and after MJD 57,040. Their power spectra are shown in Figures 2(b) and (c), respectively. It is found that the periodicity is more significant when we only used the data before MJD 57,040. The resulting best frequency is $f_{\text{before}} = 5.076774(7) \times 10^{-5} \,\text{Hz}$ (in period $P_{\text{before}} = 0.227980(8) \text{ days}$) at $\chi^2 = 28.5$ with two degrees of freedom. The significance is \sim 4.97 σ . On the other hand, the data after MJD 57,040 show no periodicity. Apart from the Rayleigh test, we have also performed the period search using the H-test (de Jager et al. 1989), which does not assume prior information on the light-curve shape. In this H-test, 20 maximum harmonics were used. The results from the H-test are consistent with those from the Rayleigh test. The H-statistic (de Jager & Büsching 2010) at P_{full} with the full data set is 25.2, corresponding to \sim 4.10 σ . For P_{before} along with the data before MJD 57,040, the H-statistic is 28.6, corresponding to \sim 4.40 σ . Figure 3 shows the Rayleigh test significance (in units of σ) of the orbital modulation at $P_{\text{Strader}} = 0.2279817$ days when we used data of different lengths.

⁴ Available at http://fermi.gsfc.nasa.gov/ssc/data/analysis/software/.

⁵ http://fermi.gsfc.nasa.gov/ssc/

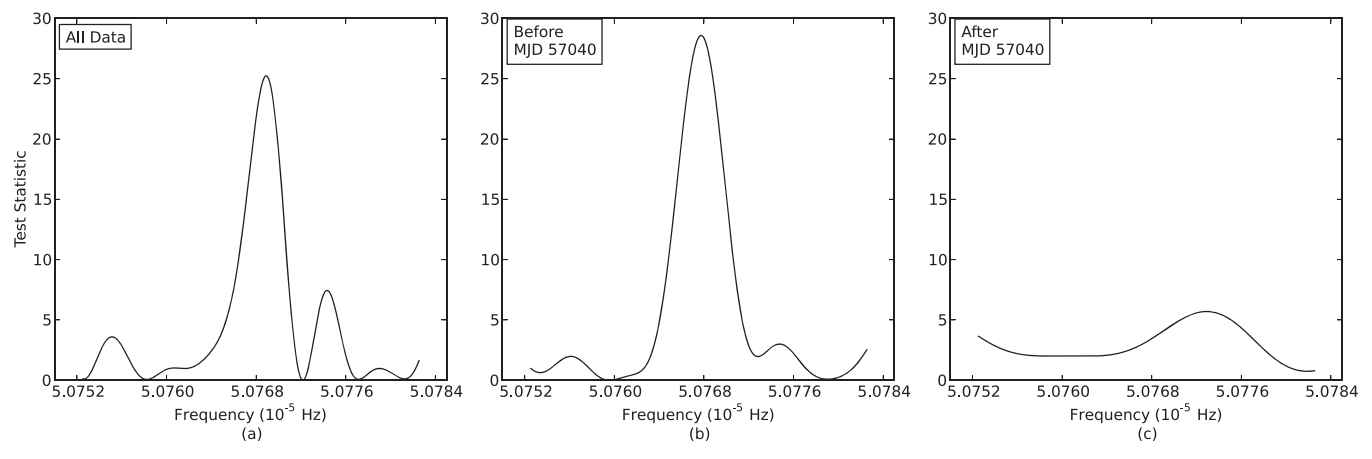


Figure 2. Rayleigh test power spectra for the whole data set (left), data that are before MJD 57,040 (middle), and data that are after MJD 57,040 (right). The y-axis indicates the χ^2 test-statistic with 2 degrees of freedom.

The horizontal x-axis marks the end date of the accumulating data. For instance, x = 55,500 (MJD) means that the test used a data set from MJD 54,682, the start of *Fermi* observation, to MJD 55,500. The maximum test-statistic is obtained when x = 57,040 at $\chi^2 = 28.3$, which is equivalent to $\sim 4.96\sigma$. On the other hand, the overall significance for the full data set at the period P_{Strader} is $\chi^2 = 18.0$, which is $\sim 3.84\sigma$. It is curious that the modulation may have been deteriorated at some point near MJD 57,000. We will discuss this in more detail in Section 3.

We constructed the gamma-ray folded light curve of 3FGL J2039.6-5618 using the orbital period from J. Strader et al. (2018, in preparation) and the two best periods in our searches using the full data and the data before MJD 57,040. The phase zero is defined to be the epoch of the optical maximum ($T_0 = 57,603.95787$ in MJD). In order to maximize the signal-to-noise ratio, we use the method of photon weighting (Kerr 2011) instead of an aperture selection to produce the folded light curve. The probability that the photon is emitted by 3FGL J2039.6-5618 is assigned to each of the photons using gtsrcprob in the Science Tools. The orbital phase is calculated using the TEMPO2 package (Hobbs et al. 2006) with the Fermi pulg-in (Ray et al. 2011). In the timing model, we adopted the main-sequence/pulsar binary model (MSS; Wex 1998). Using the photon probabilities as the weights, the resulting weighted light curves are shown in Figure 4. From top to bottom, the orbital periods used in folding the light curves are $P_{\rm Strader}=0.22798177$ days, $P_{\rm full}=0.2279757$ days, and $P_{\rm before}=0.2279808$ days, respectively. Two orbital periods are shown for clarity. The light curve indicates that the modulation is a single peak. The FWHM of the peak spans from about $\phi = 0.25$ to $\phi = 0.7$, which occupies almost half of the orbital period. Although the best period found from the Rayleigh test has different values with different time spans, the folded light curves in Figure 4 generally show similar signal structures. As we speculate that the gamma-ray modulation disappears after MJD 57,040, it is not reliable to use the best period P_{full} obtained from the full data set, which includes the no-signal duration. On the other hand, the best period P_{before} is obtained from the data only containing the portion before MJD 57,040; therefore, it may be biased to be applied to the study of the full data set. Therefore, with a negligible difference in the light curves and modulation significances ($\chi^2(P_{\text{before}}) = 28.5$ vs. $\chi^2(P_{\text{Strader}}) = 28.3$ for

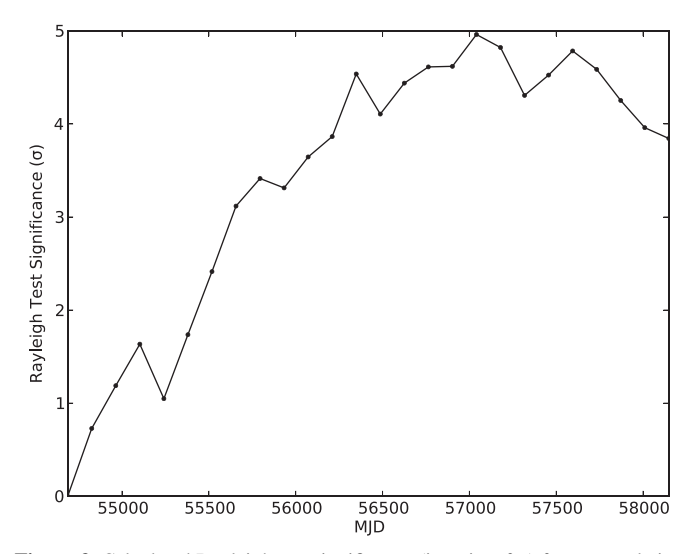


Figure 3. Calculated Rayleigh test significance (in units of σ) for accumulating data. The time shown in the horizontal axis means the time that the data used in the test are up to. For instance, the data span from MJD 54,682 to MJD 57,040 produces the highest significance (\sim 4.96 σ).

data before MJD 57,040), we adhere to the orbital period $P_B = P_{\rm Strader} = 0.2279817(7)$ days, which is reported from the independent optical observation by J. Strader et al. (2018, in preparation), for the rest of this study. Figure 5 shows the energy-dependent orbital light curves of 3FGL J2039.6–5618 in the energy ranges of 0.1–500 GeV (top), 0.1–3 GeV (middle), and 3–500 GeV (bottom). It is clear that the orbital modulation is mostly contributed by the lower part of the energy.

2.3. Orbital-phase-resolved Spectrum

We analyzed the emission spectrum of 3FGL J2039.6–5618 in different orbital phases. From the orbital light curve in Figure 4, we defined the phase interval between 0.3 and 0.8 as the inferior conjunction (INFC) and the rest of the phase interval as the superior conjunction (SUPC). The spectral form of 3FGL J2039.6–5618 is modeled by a power law with a

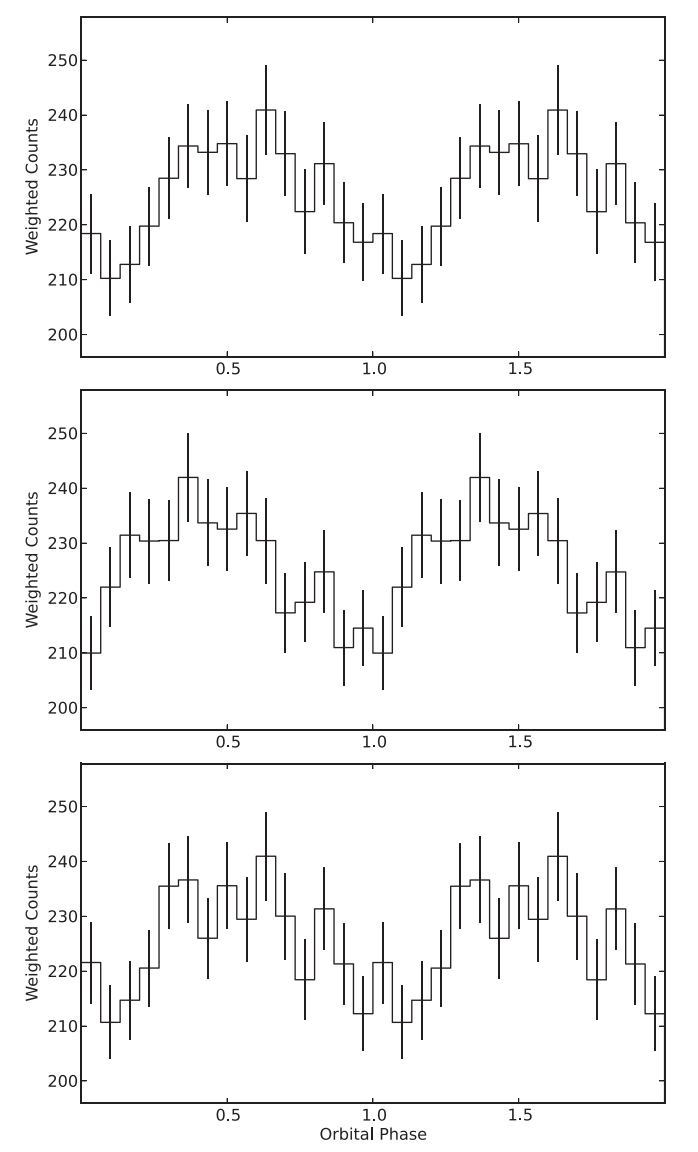


Figure 4. Gamma-ray folded light curve of 3FGL J2039.6–5618 using the full data set at different orbital periods of $P_{\rm Strader}=0.22798177$ days (top), $P_{\rm full}=0.2279757$ days (middle), and $P_{\rm before}=0.2279808$ days (bottom). The photon count in each bin is weighted by the probability that the photon is coming from the source.

simple exponential cutoff:

$$\frac{dN}{dE} = N_0 \left(\frac{E}{E_0}\right)^{-\Gamma} \exp\left(-\frac{E}{E_C}\right),\tag{1}$$

where N_0 is the normalization constant, E_0 is the scale factor of energy, Γ is the spectral power-law index, and E_C is the cutoff energy. Using binned likelihood analysis and the full data set, the best-fit parameters for INFC are $N_0 = (5.24 \pm 0.73) \times 10^{-11}$, $\Gamma = -1.58 \pm 0.11$, and $E_C = 3743 \pm 787$. For SUPC, $N_0 = (3.89 \pm 0.69) \times 10^{-11}$, $\Gamma = -1.71 \pm 0.12$, and $E_C = 6664 \pm 2075$. We also attempted to analyze the INFC and SUPC spectra using the specific data sets: before and after MJD 57,040. While the preliminary results suggest that the spectral differences for the data before MJD 57,040 are consistent with those for the full data set, the conclusion for the data after MJD 57,040 is mainly affected by the limited statistics due to low photon counts,

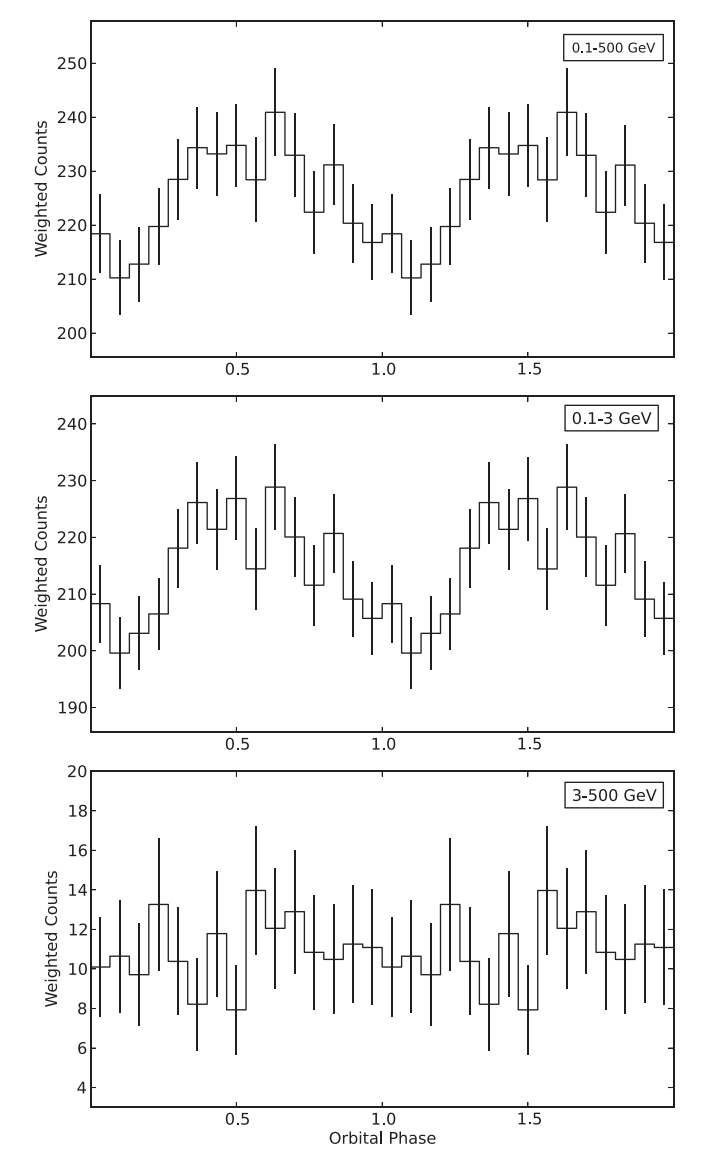


Figure 5. Energy-dependent light curve of 3FGL J2039.6–5618 as in Figure 4 folded with the orbital period $P_{\text{Strader}} = 0.22798177$ days in the energy ranges 0.1–500 GeV (top), 0.1–3 GeV (middle), and 3–500 GeV (bottom). The orbital modulation is mainly contributed by the lower-energy part.

and therefore definite perception could not be drawn at the moment. The spectral energy distributions are obtained by performing the likelihood fitting in each energy band, using a simple power-law form for 3FGL J2039.6–5618:

$$\frac{dN}{dE} = N_0 \left(\frac{E}{E_0}\right)^{-\Gamma},\tag{2}$$

where Γ is assumed to be -2.1. A 95% upper limit is derived when the test-statistic is less than 9 ($\sim 3\sigma$). The phase-resolved spectra are shown in Figure 6. In the figure, the left panel shows the best-fit spectrum during SUPC (solid line) with the corresponding uncertainty (gray shade). The spectral points are consistent with the simple power law with exponential cutoff model. The right panel shows the best-fit spectrum during INFC (dashed line) with an overlaying SUPC spectrum (solid line and gray shade). When comparing the spectra of these two phases, it is observed that the INFC phase carries an emission

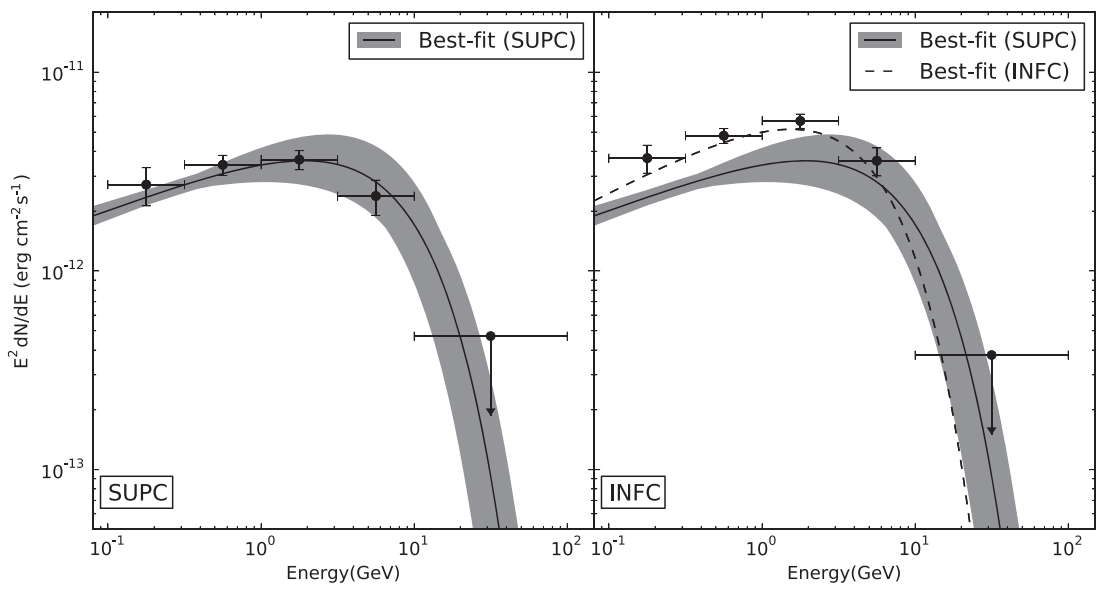


Figure 6. Orbital-phase-resolved spectra of 3FGL J2039.6–5618 during SUPC (left) and INFC (right) as described in Section 2.2. The solid (SUPC) and dashed (INFC) lines are best-fit power law with exponential cutoff models. The gray band represents the uncertainty in the best-fit spectrum of SUPC.

excess below ~ 3 GeV. We propose that the SUPC spectrum is contributed by the pulsar's magnetospheric emissions, mainly, the curvature radiation in the outer gap (Cheng et al. 1986a, 1986b). Then, the INFC spectrum is a result of an extra component added to this magnetospheric emission. This extra component has an orbital modulated property at the lower energy. The origin of this extra component will be discussed in the next section.

3. Discussion

We have reported the evidence on the orbital modulation of gamma-ray emissions from 3FGL J2039.6-5618. We have produced the pulsating light curve using the timing parameters from an optical observation. The pulsation is at a significance of $\sim 4\sigma$ level. The signal may have been interrupted beyond MJD \sim 57,000. We have analyzed the gamma-ray spectrum in the half orbital phase intervals containing the superior and inferior conjunctions, respectively. When comparing the spectra, we observed an excess of <3 GeV emission in the inferior conjunction. In this section, we will discuss the origin of this modulated emission, based on the millisecond pulsar binary scenario. We believe that it could be generated by the inverse Compton scattering between the relativistic pulsar wind particles and the soft stellar photons. This is because in this scenario the gamma-ray maximum is located around the inferior conjunction where the collision angle becomes headon. Another possible cause for gamma-ray modulations is the occultation of the gamma-ray emission by the companion star. This occultation effect can be observed in millisecond pulsar binaries such as PSR J1311-3430 (Xing & Wang 2015b) and XSS J12270–4859 (Xing & Wang 2015a). However, in the case of occultation, the gamma-ray maximum will occur at around the superior conjunction. This is contrary to the observation of 3FGL J2039.6-5618, and therefore the inverse Compton scattering is the more preferred explanation than the occultation. Here we will assume the inverse Compton model to be the sole origin for the modulation, and we will present the model details to simulate the observed data.

3.1. Pulsar Wind Emissions

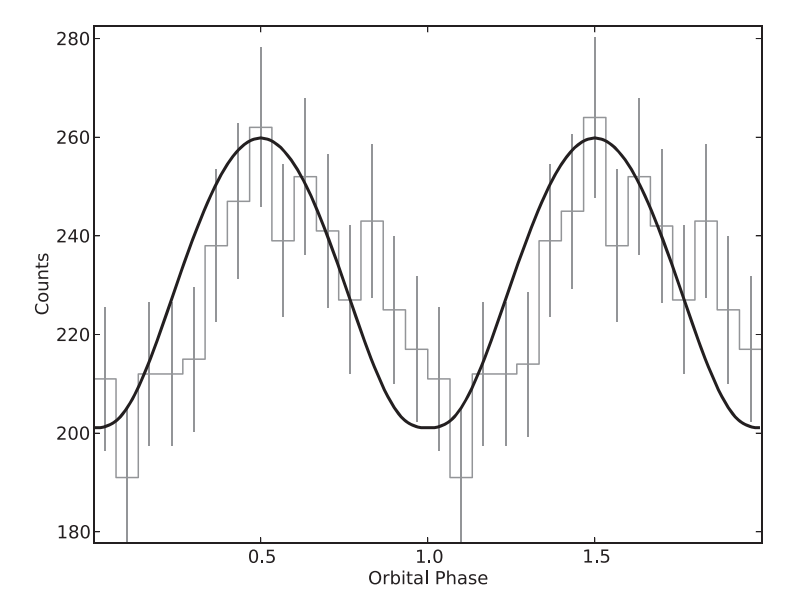
There have been studies on other gamma-ray-emitting pulsar binaries, revealing that the inverse Compton processes between the pulsar wind and the low-energy photons from a main-sequence star can produce the observed gamma-ray orbital modulation. The pulsar/Be star system PSR B1259–63 is a well-studied example where the inverse Compton scattering explains the gamma ray that is emitted around the periastron passage (Ball & Kirk 2000; Murata et al. 2003; Takata et al. 2012). The pulsar powers an energetic stream of electrons and positrons, converting the electromagnetic Poynting energy into the particle kinetic energy (Kennel & Coroniti 1984a, 1984b; Hoshino et al. 1992). The magnetization parameter σ is defined to be the ratio between the Poynting energy density and the particle kinetic energy density:

$$\sigma(r) = \frac{B^2(r)}{4\pi u_w \Gamma_w n(r) m_e c^2},\tag{3}$$

where u_W is the dimensionless radial four-velocity, Γ_W is the Lorentz factor of the particles in the pulsar wind, m_ec^2 is the rest-mass energy of electrons, and B(r) and n(r) are the magnetic field and the proper electron number density, respectively, at a distance r away from the pulsar. A power-law relation between the magnetization parameter and the radial distance has been explored to explain the orbital modulation of X-ray/TeV emission from the gamma-ray binaries (Kong et al. 2011, 2012; Takata et al. 2014, 2017). By assuming that the pulsar wind forms at the light cylinder, we explore a power-law form of

$$\sigma(r) = \sigma_L \left(\frac{r}{r_L}\right)^{-\alpha},\tag{4}$$

where σ_L is the magnetization at the light cylinder, r_L is the radius of the light cylinder, and α is the power-law index, assumed to be 1–2. By neglecting the energy loss of the pulsar wind, the sum of the kinetic energy and magnetic energy of the



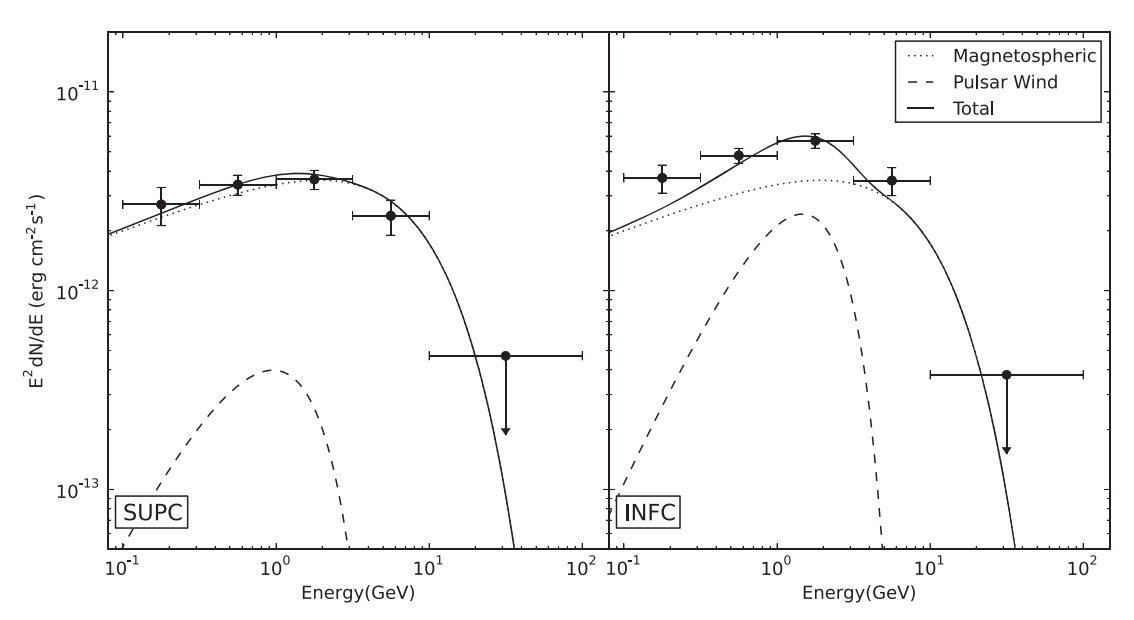


Figure 7. Comparison between the theoretical simulation and the full observational data. Top: the black curve is the simulated orbital modulating inverse Compton emission from the pulsar wind on top of a steady magnetospheric emission. The histogram shown here is produced from the photon counts (folded with the orbital phase) within a 0°6 ROI centered at the position of 3FGL J2039.6–5618. Bottom: spectra of the simulated emission in the INFC and SUPC intervals. The dotted line represents the magnetospheric emission of the pulsar, which is assumed to be in the form of the best-fit SUPC power law with exponential cutoff. The dashed line represents the pulsar wind component, which is the inverse Compton scattering with the soft photons of the companion star. The solid curve is the sum of the two components.

pulsar wind is constant with the radial distance, implying that

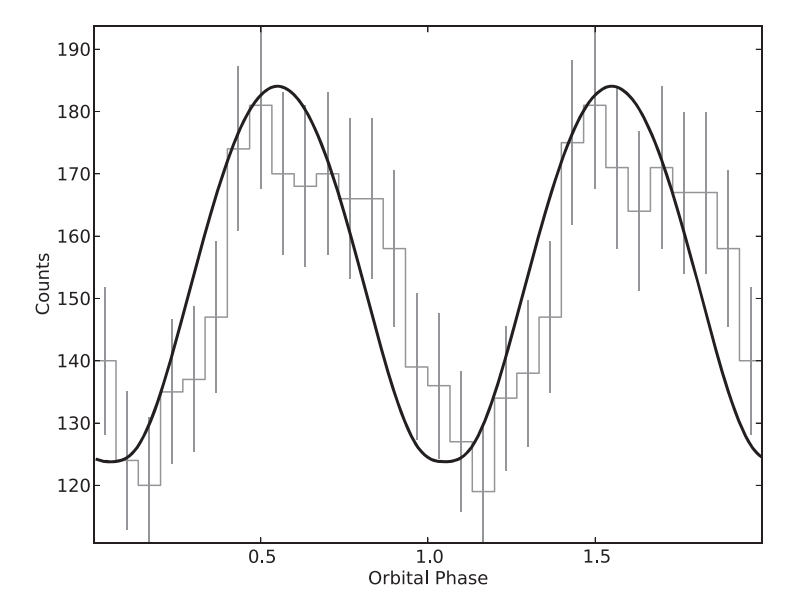
$$\Gamma_W(r)[1 + \sigma(r)] = \Gamma_{W,L}(1 + \sigma_L). \tag{5}$$

The Lorentz factor evolves as $\Gamma_W(r) \propto r^{\alpha}$ when $\sigma \gg 1$ and as the terminal Lorentz factor $\Gamma_{c,W} \sim \Gamma_{W,L}\sigma_L$ when $\sigma < 1$. The charged particles are generally accelerated to the ultrarelativistic limit $(\Gamma_W \sim 10^{4-9})$; Rees & Gunn 1974).

The black widow pulsar binary PSR B1957+20 is a more analogous system to the target of this study, 3FGL J2039.6-5618. Wu et al. (2012) analyzed the *Fermi* data on the gamma-ray emission from PSR B1957+20 and found similar orbital modulation that peaks around the inferior conjunction. The pulsar wind component mainly contributes to the emission excess above

2.7 GeV. Compared to PSR B1957+20, the companion star of 3FGL J2039.6–5618 has a lower effective temperature $T_{\rm eff}\sim 4200\,\rm K$ (Romani 2015), as $T_{\rm eff}\sim 8300\,\rm K$ for the companion of PSR B1957+20. On the other hand, 3FGL J2039.6–5618 has a shorter orbital period (J2039: 5.4 hr; B1957: 9.2 hr) and hence a smaller orbital separation. In Wu et al. (2012), the terminal Lorentz factor at $\sigma\ll 1$ is $\Gamma_{c,W}=4\times 10^4$ for PSR B1957+20. For 3FGL J2039.6–5618, we chose $\Gamma_{c,W}\sim 3\times 10^4$ to explain the spectral peak at $\sim 1\,\rm GeV$.

We have simulated the emission resulting from the inverse Compton scattering between the pulsar wind charges and the stellar soft photons. The power per unit energy per unit solid angle of the inverse Compton scattering is formulated by



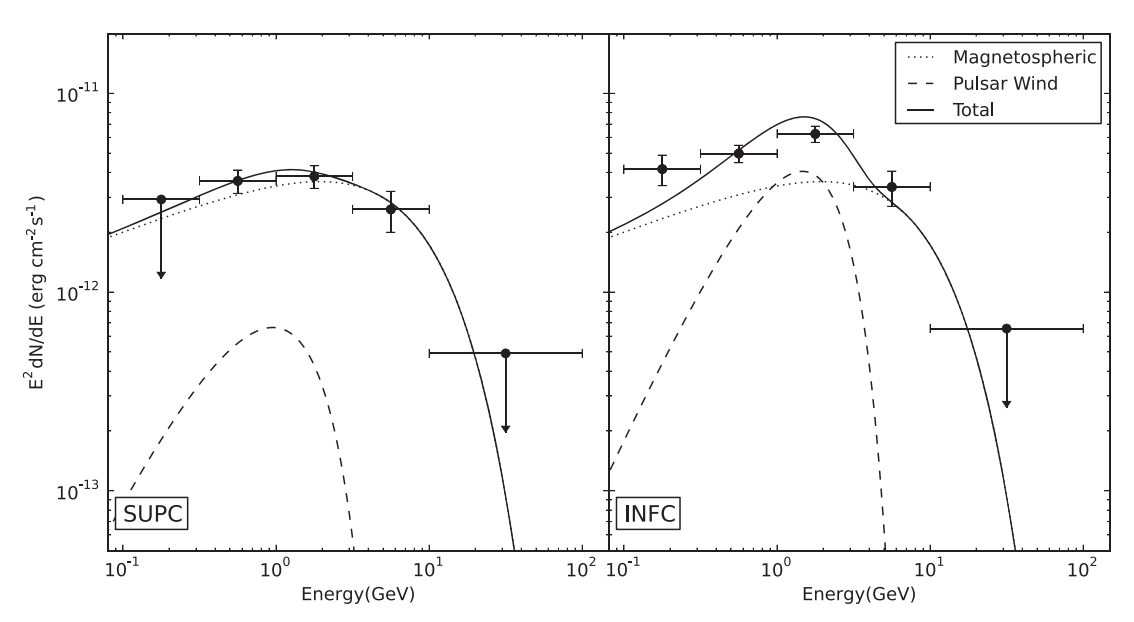


Figure 8. Similar to Figure 7, but the simulations here are fitted to the observation from MJD 54,682 to MJD 57,040 only.

Begelman & Sikora (1987) as

$$\frac{dP_{\rm IC}}{d\Omega} = \mathcal{D}^2 \int_0^{\theta_C} (1 - \beta \cos \theta_0) I_b / h \frac{d\sigma'_{\rm KN}}{d\Omega'} d\Omega_0, \tag{6}$$

where $\beta=(1-\Gamma_W^{-2})^{1/2}$, $\mathcal{D}=\Gamma_W^{-1}(1-\beta\cos\theta_1)^{-1}$, θ_0 (θ_1) is the angle between the direction of the motion of the charged particles and the stellar soft photons (the propagation direction of the scattered photon), h is the Planck constant, I_b is the intensity of the background soft photon, $d\sigma'_{\rm KN}/d\Omega'$ is the differential Klein–Nishina cross section, and θ_C is the angular size of the companion star as seen from the emission point.

We calculated the inverse Compton scattering process from the light cylinder to the radial discus of the shock with the evolutions of the magnetization described by Equations (4). The orbit of the binary system is assumed to be a circular orbit with a separation of $a=1.3\times10^{11}\,\mathrm{cm}$. We assume that the companion star fills the Roche lobe and the intrabinary shock is

located at the stellar surface. The Roche lobe radius of the companion star is taken as $R_* \sim 8 \times 10^{10}$ cm, with the mass ratio being q=0.36. We apply $T_*=4200\,\mathrm{K}$ for the temperature of the companion and D=0.5 kpc for the distance from Earth to 3FGL J2039.6–5618.

For the parameters of the pulsar, we assume a spin-down power of $L_{\rm sd} \sim 10^{35} \, {\rm erg \ s^{-1}}$ and a light-cylinder radius of $r_L = 1.5 \times 10^7 \, {\rm cm}$ for an example. The particle number density of the distance r is calculated as $n(r) = L_{\rm sd}/[4\pi r^2 m_e c^3 \Gamma_{W,L}(1+\sigma_{W,L})]$. We integrate Equation (6) to the shock distance $r_s = a - R_*$ with the effect of the anisotropic inverse Compton scattering process. We choose $\Gamma_{W,L} = 100$ and $\sigma_L = 300$ in order to provide the terminal Lorentz factor of $\Gamma_{c,W} = 3 \times 10^4$ and to produce the observed flux level with $D = 0.5 \, {\rm kpc}$ and $L_{\rm sd} \sim 10^{35} \, {\rm erg \ s^{-1}}$. The choice of $\Gamma_{W,L}$ and σ_L does not affect the results, provided that (1) the terminal Lorentz factor is $\Gamma_{W,t} \sim \Gamma_{W,L} \sigma_{W,L} \sim 3 \times 10^4 \, {\rm and}$ (2) the magnetization is $\sigma \ll 1$ at the shock, that is, the the pulsar wind almost

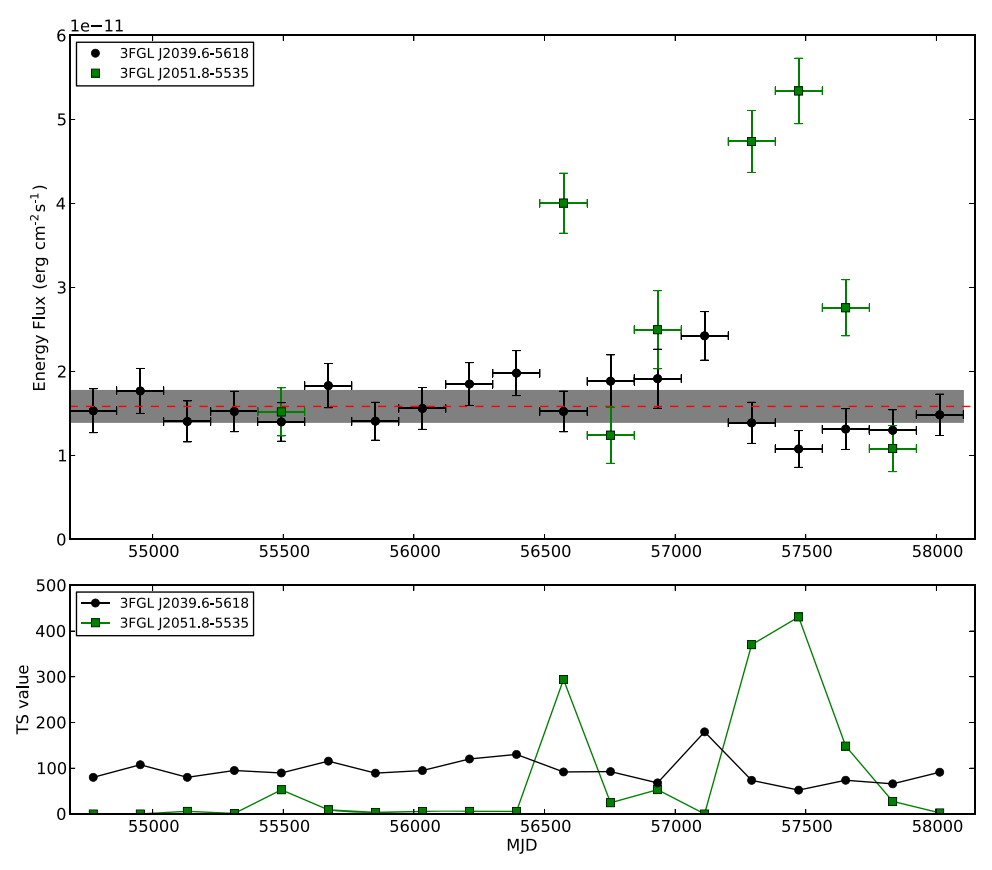


Figure 9. Top: energy flux time series of the nearby blazar candidate 3FGL J2051.8–5535 overlaid with that of 3FGL J2039.6–5618. Bottom: corresponding test-statistic (TS) values in the binned likelihood analysis. Only the points with TS > 9 ($\sim 3\sigma$) have their energy flux shown in the top panel.

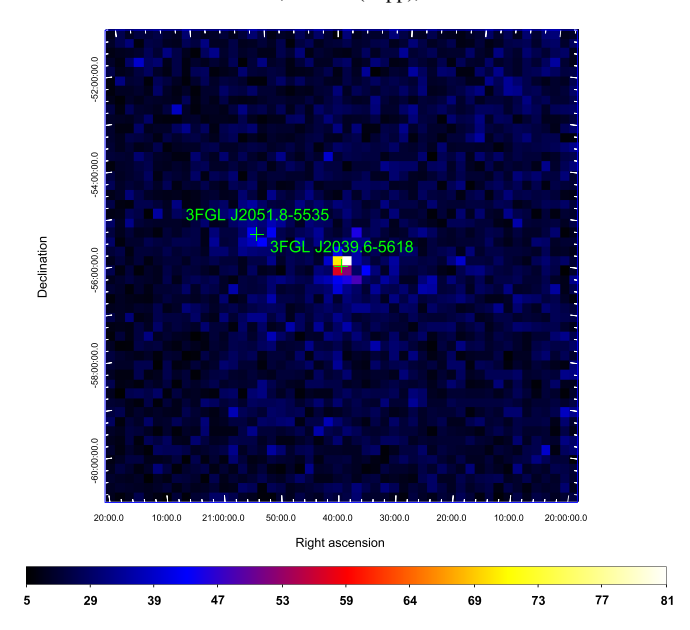
reaches to the terminal Lorentz factor at the shock. We found that if the magnetization factor is larger than unity all the way from the light cylinder to the shock, the spin-down power required to explain the observed flux level is much larger than $L_{\rm sd} > 10^{35} \, {\rm erg \ s^{-1}}$.

The results of the simulation are shown in Figure 7. The top panel shows the simulated orbital light curve. The light curve consists of a magnetospheric DC level and a pulsar wind component that is modulating. The curve is fitted to the observed folded light curve of the gamma-ray photons (0.1 MeV–500 GeV) within a 0.6 ROI centered at the position of 3FGL J2039.6–5618. The orbital phase zero, as in Figure 4, corresponds to the epoch of optical maximum at MJD 57,603.95787. As we believed, the optical maximum occurs around the SUPC because the heating side of the companion star is facing toward the observer. Therefore, the phase ~ 0.5 corresponds to the INFC where the gamma ray peaks because of the head-on collision of the inverse Compton process. The bottom panel of Figure 7 shows the simulated spectra at the SUPC and INFC intervals as labeled. The dashed line refers to the pulsar wind component, and the dotted line refers to the magnetospheric component. The magnetospheric emission from the pulsar in the gamma-ray regime is mainly contributed by the curvature radiation in the outer gap. It generally follows the form of a power law with exponential cutoff. Therefore, we use the best-fit power law with exponential cutoff function from the binned likelihood analysis to represent the spectrum of the magnetospheric emission. The pulsar wind component peaks at around 1 GeV. The characteristic energy of this component depends on the energy of the soft photons and the Lorentz factor of the pulsar

wind, as well as the scattering angle. Hence, the pulsar wind component during INFC has a higher characteristic energy than in SUPC. The component in INFC could roughly contribute a similar magnitude to the magnetospheric emission in the lower energy. Thus, it produces an excess in the lower energy of the gamma-ray spectrum. A similar result is presented in Figure 8 for simulating the gamma-ray modulation and spectrum in the signal-on period before MJD 57,040. When we only use the data before MJD 57,040, as we discussed in Section 2.2, the modulation has shown a larger significance. Therefore, the light curve in the top panel shows a variation amplitude of about 50%. In the spectrum, the peak emission of the pulsar wind component is comparable to the strength of the magnetospheric emission at $\sim 1~\rm GeV$.

3.2. Loss of Orbital Modulation after MJD ~57,000

From the results in the previous section, we can see that in the case of 3FGL J2039.6–5618, the inverse Compton scattering in the binary can explain the modulating feature and the observed excess in the gamma-ray spectrum. Besides, we have mentioned in Section 2.2 and Figure 2 that there may be a disappearance of the orbital modulation around MJD 57,000. One possible explanation suggests that there may be a change in the relative strengths between the pulsar wind and the stellar wind. In the X-ray and optical observations by Salvetti et al. (2015), it is seen that the X-ray light curve peaks around the optical maximum. This indicates that the companion stellar wind is stronger than the pulsar wind in this system. Therefore, the shock cone is opening toward the pulsar. If the stellar wind gets stronger (or the pulsar wind becomes weaker),



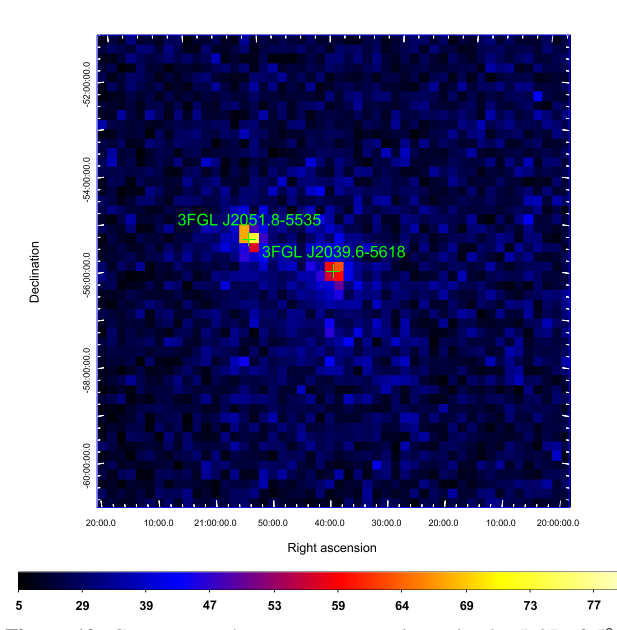


Figure 10. Gamma-ray photon count maps in a circular ROI of 5° radius centered at 3FGL J2039.6–5618 using the data during MJD 55,932–57,040 (top) and MJD 57,040–58,148 (bottom). The color bars are tuned to have the same scale showing the number of detected photons in each $0.2^{\circ} \times 0.2^{\circ}$ pixel.

the radius of the cone of the shock will be suppressed and the shock will be located at a closer distance to the pulsar. If the shock occurs at half of the original distance, the emission region and hence the flux are reduced to be a half, which makes the detection of the pulsation harder. For $\sigma\gg 1$, moreover, since the Lorentz factor of the accelerated particles in the pulsar wind is increasing with the distance from the pulsar, i.e., $\Gamma_W \propto r^\alpha$, this implies that the energy of the scattered photons from the inverse Compton process becomes lower. In particular, if the shock occurs at half of the original distance, $\Gamma_W \sim 5 \times 10^3$, the typical energy of the inverse Compton component can be estimated by $\sim 3\Gamma_W^2 k T_{\rm eff} \sim 25 (T_{\rm eff}/4000) (\Gamma_W/5 \times 10^3)$ MeV. Together with the lower soft photon density near the pulsar, it would be very hard to detect this inverse Compton emission in the *Fermi* data. To confirm this scenario, the most updated X-ray observations will be

useful to check whether the radius of the shock cone has changed, since the size is related to the separation between the two peaks in the X-ray pulsation profile.

Last but not least, though less likely, the nearby gamma-ray sources close to 3FGL J2039.6-5618 may have some effect on the analysis results. Particularly, 3FGL J2051.8-5535 is a blazar candidate located ~1.8 away that has shown a giant hard gamma-ray flare from MJD \sim 57,200 to \sim 57,700 (Carpenter et al. 2015). In our likelihood analysis, we also noticed the large boost in the energy flux of 3FGL J2051.8-5535 during the period of study. Figure 9 shows the comparison of the energy flux and detection test-statistic (TS) time series between 3FGL J2039.6-5618 (circle) and 3FGL J2051.8-5535 (square). The field of view before and after the flaring can also be visualized as in the photon count maps shown in Figure 10. The same data length has been chosen in generating these two count maps to ensure that the observed photon counts are comparable. Here, we can see that the brightening of 3FGL J2051.8-5535 has reached a similar level to 3FGL J2039.6-5618. In this study, we have set the parameters for this source free in the likelihood analysis. By the nature of likelihood optimization, the probability of the photon identification has been maximized. In other words, the photons assigned to our target, 3FGL J2039.6-5618, have lower probability of coming from the blazar. However, it is not guaranteed that none of the photons from this source are mistaken to be the photon of 3FGL J2039.6–5618. Therefore, multiwavelength studies remain a better strategy to confirm any change that occurred in 3FGL J2039.6-5618.

We appreciate the anonymous referee for the constructive suggestions and comments. We also thank P. M. Saz Parkinson and J. Li for useful discussions and advice on the timing analysis. C.W.N. and K.S.C. are supported by GRF grant 17302315. J.T. is supported by NSFC grants of the Chinese Government under 1573010, U1631103, and 11661161010. J.S. acknowledges support from a Packard Fellowship. This work was partially supported by NASA grants NNX15AU83G and 80NSSC17K0507 and NSF grant AST-1714825. We also acknowledge the use of the public data and software facilities from the *Fermi* FSSC, managed by the HEASARC at the Goddard Space Flight Center.

ORCID iDs

C. W. Ng https://orcid.org/0000-0003-2584-4747
J. Takata https://orcid.org/0000-0002-8731-0129
J. Strader https://orcid.org/0000-0002-1468-9668
K. L. Li https://orcid.org/0000-0001-8229-2024

References

```
Acero, F., Ackermann, M., Ajello, M., et al. 2015, ApJS, 218, 2
Ball, L., & Kirk, J. G. 2000, APh, 12, 335
Begelman, M. C., & Sikora, M. 1987, ApJ, 322, 650
Brazier, K. T. S. 1994, MNRAS, 268, 709
Carpenter, B., Magill, J., & Ojha, R. 2015, ATel, 8096, 1
Chen, H.-L., Chen, X., Tauris, T. M., & Han, Z. 2013, ApJ, 775, 27
Cheng, K. S., Ho, C., & Ruderman, M. A. 1986a, ApJ, 300, 500
Cheng, K. S., Ho, C., & Ruderman, M. A. 1986b, ApJ, 300, 522
de Jager, O. C., & Büsching, I. 2010, A&A, 517, L9
de Jager, O. C., Raubenheimer, B. C., & Swanepoel, J. W. H. 1989, A&A, 221, 180
Hobbs, G. B., Edwards, R. T., & Manchester, R. N. 2006, MNRAS, 369, 655
```

81

```
Kennel, C. F., & Coroniti, F. V. 1984a, ApJ, 283, 694
Kennel, C. F., & Coroniti, F. V. 1984b, ApJ, 283, 710
Kerr, M. 2011, ApJ, 732, 38
Kong, S. W., Cheng, K. S., & Huang, Y. F. 2012, ApJ, 753, 127
Kong, S. W., Yu, Y. W., Huang, Y. F., & Cheng, K. S. 2011, MNRAS, 416, 1067
Murata, K., Tamaki, H., Maki, H., & Shibazaki, N. 2003, PASJ, 55, 467
Ray, P. S., Kerr, M., Parent, D., et al. 2011, ApJS, 194, 17
Rees, M. J., & Gunn, J. E. 1974, MNRAS, 167, 1
```

Romani, R. W. 2015, ApJL, 812, L24
Salvetti, D., Mignani, R. P., Luca, A. D., et al. 2015, ApJ, 814, 88
Takata, J., Leung, G. C. K., Tam, P. H. T., et al. 2014, ApJ, 790, 18
Takata, J., Okazaki, A. T., Nagataki, S., et al. 2012, ApJ, 750, 70
Takata, J., Tam, P. H. T., Ng, C. W., et al. 2017, ApJ, 836, 241
Wex, N. 1998, MNRAS, 298, 67
Wu, E. M. H., Takata, J., Cheng, K. S., et al. 2012, ApJ, 761, 181
Xing, Y., & Wang, Z. 2015a, ApJ, 808, 17
Xing, Y., & Wang, Z. 2015b, ApJL, 804, L33